Chemical Science

ROYAL SOCIETY OF CHEMISTRY

EDGE ARTICLE

View Article Online
View Journal | View Issue

Cite this: *Chem. Sci.*, 2020, **11**, 9665

All publication charges for this article have been paid for by the Royal Society of Chemistry

Quantum-mechanical transition-state model combined with machine learning provides catalyst design features for selective Cr olefin oligomerization†

Steven M. Maley, ‡[a] Doo-Hyun Kwon, ‡[a] Nick Rollins,[a] Johnathan C. Stanley,[a] Orson L. Sydora,[b] Steven M. Bischof *[b] and Daniel H. Ess *[a]

Received 27th June 2020
Accepted 20th August 2020

DOI: 10.1039/d0sc03552a

rsc.li/chemical-science

The use of data science tools to provide the emergence of non-trivial chemical features for catalyst design is an important goal in catalysis science. Additionally, there is currently no general strategy for computational homogeneous, molecular catalyst design. Here, we report the unique combination of an experimentally verified DFT-transition-state model with a random forest machine learning model in a campaign to design new molecular Cr phosphine imine (Cr(P,N)) catalysts for selective ethylene oligomerization, specifically to increase 1-octene selectivity. This involved the calculation of 1-hexene : 1-octene transition-state selectivity for 105 (P,N) ligands and the harvesting of 14 descriptors, which were then used to build a random forest regression model. This model showed the emergence of several key design features, such as Cr–N distance, Cr–α distance, and Cr distance out of pocket, which were then used to rapidly design a new generation of Cr(P,N) catalyst ligands that are predicted to give >95% selectivity for 1-octene.

Introduction

Computational chemistry now plays an active role in molecular catalyst design and optimization by either testing chemical hypotheses or directly evaluating catalyst candidates.[1] However, no general strategy for virtual catalyst design or optimization has emerged,[2–14] and there are only a few cases of specific catalyst prediction followed by experimental realization.[15–20] Due to the complex electronic structure of metal centers and ligands, one strategy for computational, homogeneous, molecular catalyst design is to use quantum-mechanical methods to model transition states.[21–27] While quantum-mechanical transition states can often replicate experiment and be used for catalyst prediction, it is not always straightforward to identify simple chemical features that control catalysis,[28,29] especially for selectivity where small energy quantities can impart significant influence. In this type of scenario, a catalyst design workflow that combines quantum-mechanical transition state modeling with machine learning has the potential to reveal critical catalyst design features not readily identified through other means.

We recently reported the development and use of a density functional theory (DFT) transition-state model that provided quantitative prediction of molecular Cr catalysts for controllable selective ethylene trimerization and tetramerization (Scheme 1).[30] This selective catalyst design effort is important because the ubiquity of polyethylene resulting from robust Phillips[31] and Ziegler–Natta catalysts[32,33] has led to an increase in global need for linear α-olefin (LAO) polymerization comonomers.[34] Additionally, these short-chain LAOs, specifically 1-hexene and 1-octene, are used in the manufacture of plasticizers, lubricants, detergents, and plastomers/elastomers. Prior to our work, Sydora and co-workers reported a series of aryl and benzyl substituted phosphine imine (P,N) catalysts that experimentally produced ~30% 1-octene.[35] In our computational catalyst design effort, we used the cationic high-spin transition-states **TS1** and **TS2** shown in Scheme 1b to develop a linear correlation model between DFT computed values and experimental 1-hexene : 1-octene ratios (see later Scheme 2 for complete catalytic cycle). This allowed using transition-state calculations to computationally design a new general class of phosphine monocyclic imine Cr(P,N) catalysts where changes in the ligand structure control 1-hexene *versus* 1-octene selectivity (Scheme 1b). Experimental ligand and catalyst synthesis, and reaction testing, quantitatively confirmed our transition-state predictions.

While our DFT transition-state model is practical, accurate, and successfully identified new ligands that were

[a]*Department of Chemistry and Biochemistry, Brigham Young University, Provo, Utah, 84602, USA. E-mail: dhe@chem.byu.edu*

[b]*Research and Technology, Chevron Phillips Chemical Company LP, 1862, Kingwood Drive, Kingwood, Texas 77339, USA. E-mail: bischs@cpchem.com*

† Electronic supplementary information (ESI) available. See DOI: 10.1039/d0sc03552a

‡ Authors contributed equally to this work.

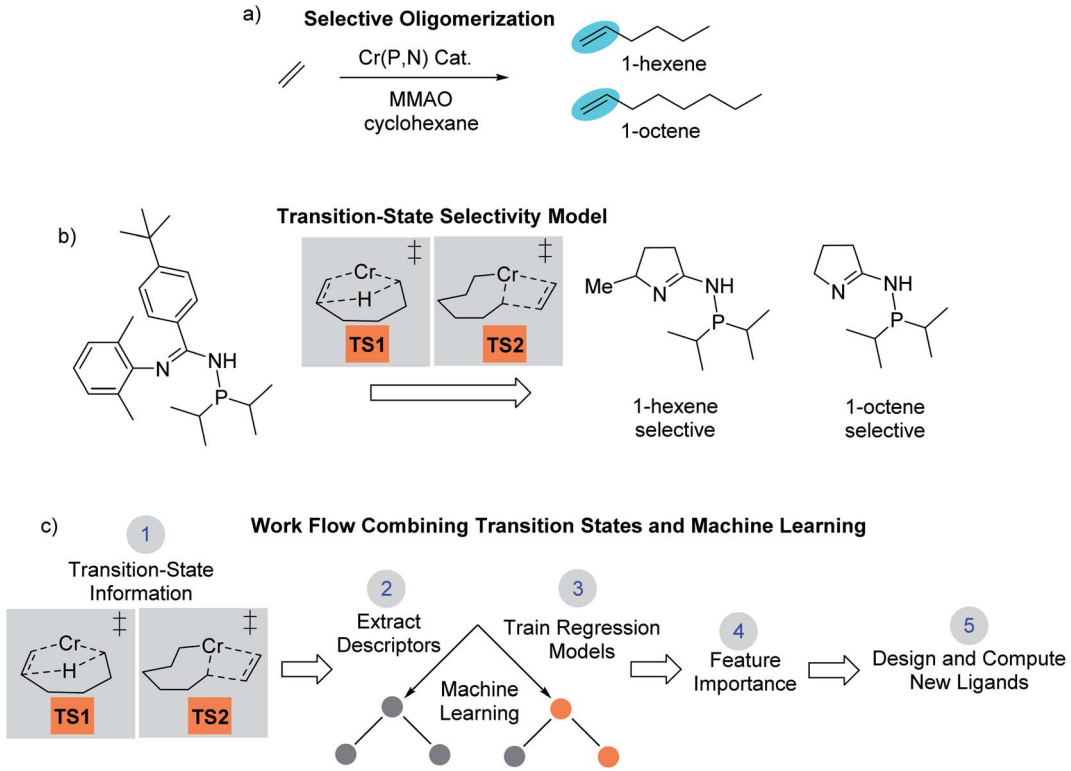

Scheme 1 (a) Outline of Cr catalyzed selective ethylene oligomerization reaction conditions with targets of 1-hexene and 1-octene. The catalyst involves a Cr metal center with phosphine and imine ligand coordination. MMAO is typically used to activate the pre-catalyst complex. (b) Outline of using TS1 and TS2 as a selectivity model to design new monocyclic imine Cr(P,N) catalysts that are 1-hexene and 1-octene selective. (c) The work presented here involves using our 1-hexene/1-octene transition-state selectivity model combined with machine learning models to reveal selectivity controlling features that are then used for virtual design of new catalyst ligands.

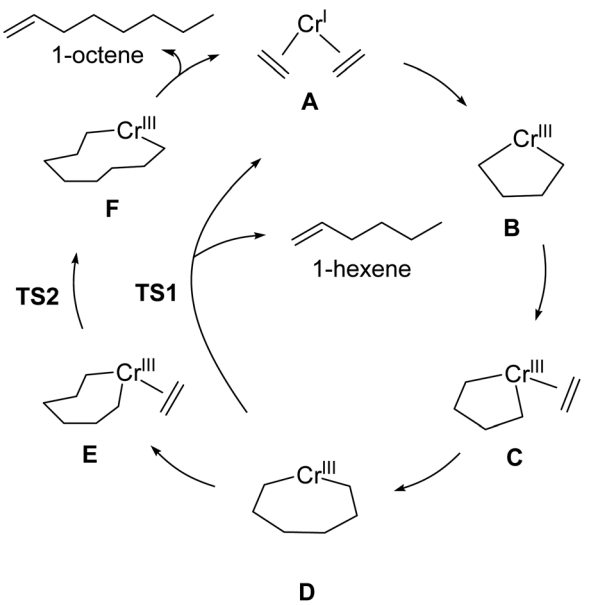

Scheme 2 Outline of Cr-catalyzed metallacycle mechanism for selective ethylene oligomerization to 1-hexene and 1-octene.

experimentally validated, it did not offer general or specific catalyst design guidance to further enhance 1-octene selectivity. Moreover, the interpretation of singular controlling transition-state features is unobvious since the energy difference between 1-hexene and 1-octene selectivity is relatively small. Therefore, we decided to combine our transition-state model with data science methods that can potentially provide the emergence of chemical features to enhance 1-octene selectivity. While machine learning and related multi-dimensional methods are beginning to be used for molecular catalyst design,[36] there are currently no examples of an experimentally verified quantum-mechanical transition state model merged with machine learning methods for catalyst selectivity. Contemporary to our work, Balcells and Azpuru-Guzik very recently reported combining machine learning and transition states for analysis of stoichiometric H_2 oxidative addition reactivity by Vaska-type complexes.[37] Currently, our work reported here and the work of Balcells and Azpuru-Guzik represent the only reports of uniquely combining transition states and machine learning. Generally, data science approaches to molecular catalyst design emphasize ground-state properties of either pre-catalysts or ligands without metal centers. For example, Fey and Pringle developed databases of ground-state ligand properties[38–43] that enabled the prediction and experimental verification of new fluorophosphine ligands for hydroformylation and hydrocyanation.[44] Recently, Denmark reported a workflow where a subset of a library of synthetically accessible catalysts are selected and tested. The data obtained was then used to train statistical learning models to optimize a chiral

catalyst for thiol addition to *N*-acylimines.[45] Machine learning methods have also been used to predict reaction barrier heights in heterogeneous catalyst applications.[46–48]

Outlined in Scheme 1c, our approach reported here involves using DFT-computed transition-state features and selectivities for machine learning analysis. The analysis of >100 Cr(P,N) catalysts and 14 molecular descriptors through machine learning regression algorithms with multifold cross validation resulted in a low root mean square error (RMSE) and emergence of three critical design elements to enhance 1-octene selectivity. The utility of these machine-learning identified selectivity features was demonstrated by the design and calculation of several new ligands that are predicted to give >90% 1-octene selectivity.

Results and discussion

Companies such as Shell, Ineos, Idemitsu, SABIC, and Chevron Phillips Chemical Company LP (Chevron Phillips Chemical) use metal-catalyzed ethylene oligomerization to produce a wide distribution of LAOs from 1-butene to 1-eicosene (C_{20}).[49] Chevron Phillips Chemical was the first to commercialize a selective ethylene trimerization to 1-hexene system using Cr(III) 2-ethylhexanoate along with 2,5-dimethylpyrrole and aluminum co-activators.[50] Sasol later developed selective ethylene oligomerization technology that produces both 1-hexene and 1-octene using a Cr-diphosphinoamine catalyst.[51] However, an important and major unsolved challenge is to develop a general set of molecular catalysts and catalyst design principles that result in highly selective ethylene tetramerization to 1-octene.

As discussed in the introduction, in our recent computational campaign, we developed a DFT transition-state model that provided quantitative prediction of molecular Cr(P,N) catalysts (Scheme 1).[30] This resulted in the computational design and experimental verification of a new general class of phosphine monocyclic imine Cr(P,N) catalysts where slightly more than 50% 1-octene was formed. Importantly, this DFT transition-state model is accurate and relatively fast to use. New ligands can be virtually screened by calculating the energies of transition-state conformation ensembles for **TS1** and **TS2** (Scheme 1b),[52–63] which can then be used in our linear correlation model to provide a predicted 1-hexene : 1-octene ratio for given set of reaction conditions. Our transition-state selectivity model was based on our DFT mechanistic calculations, and studies by Britovsek and McGuinness, Cheon, Liu and others.[52,53,56–63] Briefly, pre-catalyst activation results in a bis-ethylene Cr^{I} species **A** and oxidative C–C bond formation then results in chromacyclopentane **B** (Scheme 2). A third ethylene coordination gives **C** and migratory insertion leads to the chromacycloheptane intermediate **D** where 1-hexene and 1-octene pathways diverge. Through β-hydrogen transfer **TS1** there is formation of 1-hexene and Cr catalyst reduction. The 1-octene pathway requires a fourth ethylene coordination and intermediate **E** followed by migratory insertion **TS2** to give the chromacyclononane intermediate **F** that leads to 1-octene.

While our DFT transition-state model is extremely useful, because it is a correlation model with small energy differences, it did not reveal general catalyst design principles that would easily lead to the design of extremely high 1-octene selectivity. Because our transition-state selectivity model is accurate, this provided a platform for combining it with machine learning data science methods that can provide the emergence of general chemical features to enhance 1-octene selectivity for Cr(P,N) catalysts. To our knowledge, there has not been a previous report of combining an experimentally verified quantum mechanical transition-state model for selectivity with machine learning analysis as a workflow to design new catalysts.

While machine learning is beginning to find significant application as a tool to aid organic synthesis,[64–74] there are relatively few examples of machine learning applied to inorganic or organometallic reactions, especially heterogeneous[46,75–87] and homogeneous catalysis.[88,89] Kulik trained an artificial neural network to predict the high-spin to low-spin splitting energies of ~2700 transition metal complexes.[90] They also demonstrated the usage of a kernel ridge regression model for predicting spin-splitting, bond lengths, and redox potentials for a relatively large collection of transition metal complexes.[91] Related, Corminbouef trained machine learning models to screen over 18 000 potential homogeneous catalysts for the Suzuki–Miyaura C–C cross-coupling reaction.[92] Sunoj used a combination of a neural network and random forest model to identify the regioselectivity of catalytic difluorination of alkenes.[93] Brgoch screened over 100 000 compounds using a support vector machine regression to identify novel highly compressible metal materials,[94] and Buehler used convolutional neural networks to search for new composite metal materials.[95] Xin used artificial neural networks to identify heterogeneous metallic catalysts for CO capture and reduction.[96] Most directly related to our work, a recent and important contribution by Balcells and Azpuru-Guzik demonstrated the use of machine learning for reactivity to screen ligands of Vaska-type complexes to identify optimal ligands for H_2 oxidative addition. This work showed that machine learning

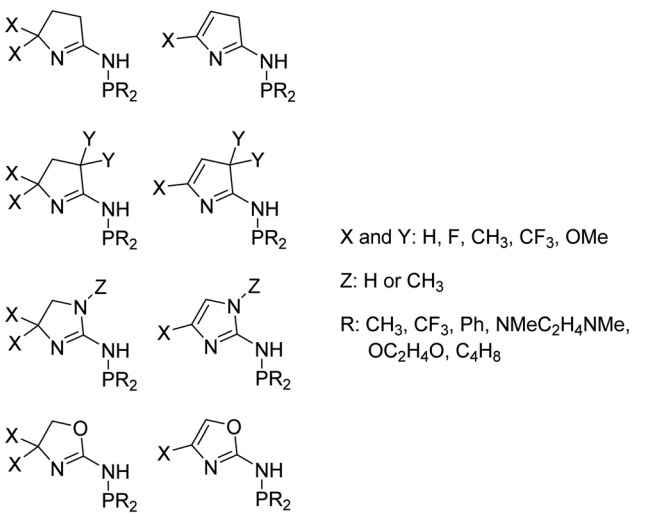

Scheme 3 Outline of 105 unique (P,N) ligands in our transition-state training data set. These ligands were used to calculate selectivity based on **TS1** and **TS2**. Transition-state features were then harvested from the electronic structure and geometries of **TS1** and **TS2**.

identified atom size and electronegativity as key features impacting H_2 oxidative addition reactivity.[37]

With the success of previous machine learning studies predicting spin-splitting energies and redox potentials,[90,91] we were relatively confident that one or more machine learning algorithms would perform well for our workflow. Similar to our previous computational studies,[30] and computational assessments by McGuinness suggesting the good performance of M06L,[52,53] we used the unrestricted M06L density functional[97] for describing the electronic structure of Cr(P,N) catalysts. The UM06L/Def2-TZVPP//UM06L/6-31G**[LANL2DZ] level of theory was combined with the SMD continuum model[98] for cyclohexane to estimate the free energies of **TS1** and **TS2** (see ESI† for computational details). In this transition state model, the relative free energies of **TS1** and **TS2** provide selectivity under the assumption of Curtin–Hammett type conditions. All transition-state structures were optimized, and vibrational frequencies were computed to verify the stationary points as first-order saddle points. Normal rigid-rotor harmonic oscillator approximations were applied with free energies at 1 atm and 298 K. Because the transition-state model is a linear correlation scheme, no temperature or pressure corrections were applied. All DFT calculations were performed using Gaussian 09.[99] Machine learning analyses were performed using scipy,[100] numpy,[101] pandas[102] and scikit-learn[103] in Python 2.7. A detailed description of the machine learning analysis along with the source code are available in the ESI.†

We used 105 unique (P,N) ligands in our transition-state training data set, which included 14 experimentally measured ligands. Scheme 2 outlines these (P,N) ligands, which have a variety of different functional groups, but retain the phosphine and imine, or imine-like, ligand coordination for which the DFT transition-state model was developed. A major motivation in the selection of these 105 ligands was to further optimize the five-membered imine ring system we previously designed and to stay within the bounds of predictability for our correlation model. As shown in Scheme 3, this set includes a variety of substituted heterocycles such as pyrroles, imidazoles, and oxazoles. In each of these cases we also examined their combination with alkyl, fluoroalkyl, aryl, and amido phosphines as well as phospholanes.

Fourteen atomic and molecular descriptors/features were extracted from **TS1** and **TS2** for each of the 105 ligands shown in Scheme 3. Described in Fig. 1, extracted features included geometric parameters such as bond lengths, angles, dihedrals, percent volume buried, and Cr metal center distance out pocket. Several electronic features were also harvested, such as electrostatic-based atomic charges. Percent volume buried

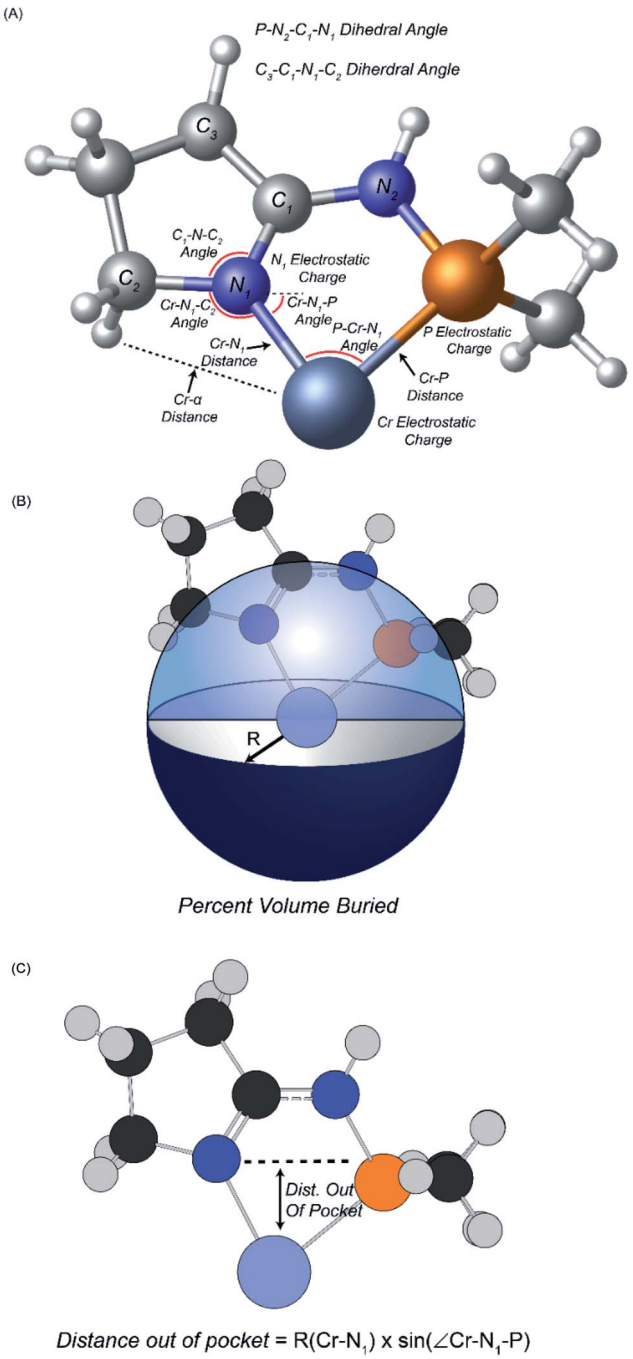

Fig. 1 Descriptors extracted for machine learning analysis. (A) Geometric descriptors and electrostatic charges. (B) Definition of percent volume buried. (C) Definition of distance out of pocket.

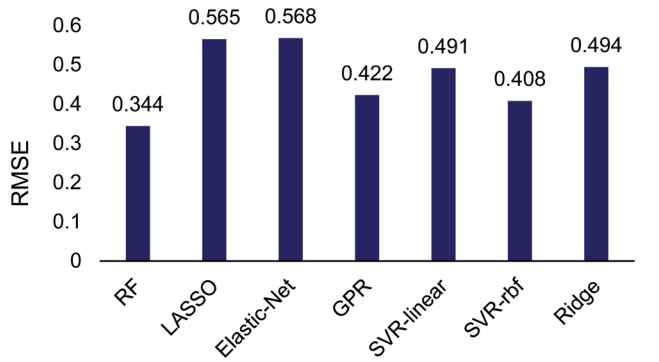

Fig. 2 Root mean square error (RMSE) for machine learning regression algorithms to quantitatively predict TS1 and TS2 energy differences using 14 atomic and molecular features. RF = random forest, LASSO = least absolute shrinkage and selection operator, GPR = Gaussian process regression, SVR = support vector regression.

describes the extent to which the first coordination sphere of the Cr metal center is occupied by a (P,N) ligand.[104] The distance out of pocket describes the how far the Cr metal is situated from the (P,N) ligand.

The Scikit-Learn python library was used to set up and train regressors on this transition-state data set, which was split into 25% training and 75% testing sets. Seven regression algorithms were tested including: random forest, Gaussian process

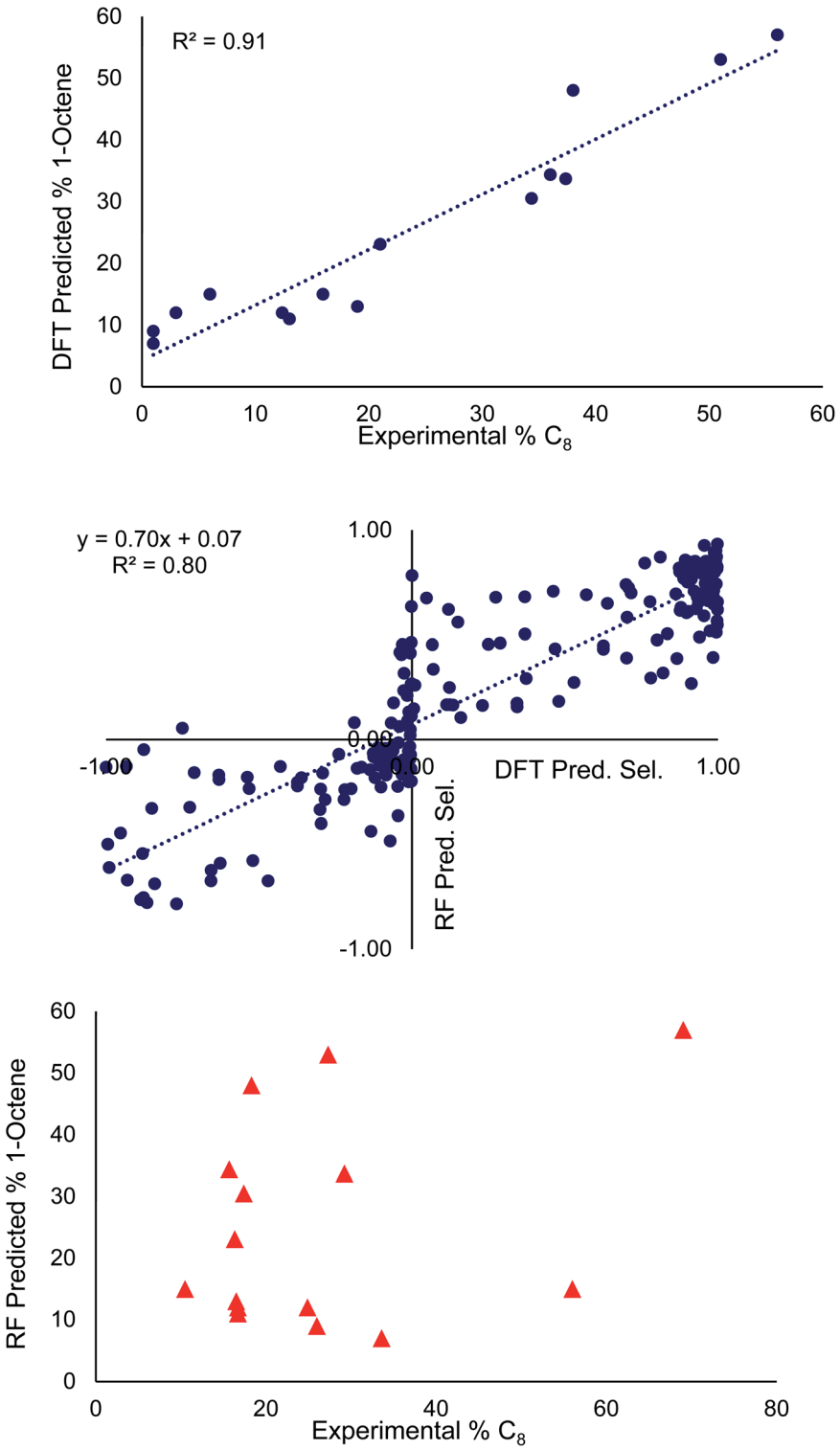

Fig. 3 Top: Linear regression of 1-octene selectivities predicted by DFT selectivity model compared to experimental values. Middle: Linear regression of selectivities predicted by DFT selectivity model (x-axis) and optimized random forest (RF) model (y-axis). Negative values correspond to high 1-hexene selectivity, positive values to high 1-octene selectivity. Bottom: Linear regression of 1-octene selectivities predicted by random forest models compared to experimental values.

regression, LASSO, elastic-net, ridge regression and support vector regression with both a linear and radial basis function kernel. Multifold cross validation was performed to protect against model overfitting common in small datasets. This random sampling was performed 10 times and 20-fold cross validation was used at each iteration to determine regression accuracy. A brief test of different amounts of random sampling and cross validation was also performed (see ESI†). The RMSE of each model determined using cross validation averaged across iterations is shown in Fig. 2.

The machine learning regression algorithms were used to evaluate the use of the 14 atomic and molecular features to quantitatively correlate with the DFT calculated energy differences between **TS1** and **TS2**. The RMSE of the regression algorithms ranged from 0.344 to 0.568 (Fig. 2). The best performing model was random forest (RMSE = 0.344) and the poorest performing model was elastic-net (RMSE = 0.568). Unsurprisingly the LASSO and ridge algorithms, which are related to elastic-net, also performed poorly with RMSEs of 0.565 and 0.494, respectively. The performance of support vector regression improved by almost 10% when changing from a linear (RMSE = 0.491) to a radial basis function (RMSE = 0.408) kernel. Gaussian process regression performed comparable to SVR-rbf.

Related to the top performance of random forest for our correlation of 1-hexene : 1-octene ratios, Doyle reported that random forest outperformed linear models, SVR, k-nearest neighbor, and artificial neural networks at predicting yields of Pd-catalyzed Buchwald–Hartwig cross-coupling of aryl halides with 4-methylaniline.[70] Also, for spin-splitting energies and bond lengths of transition metal complexes, Kulik achieved exceptionally low mean unsigned errors using random forest.[91] Palmer *et al.* showed that random forest outperforms SVR and artificial neural networks in predicting the aqueous solubility of organic molecules.[105]

Because the random forest algorithm performed well in our case, and the applications mentioned above, this algorithm was chosen for further hyperparameter optimization using the GridSearch CV method from SciKit-Learn. Different permutations of hyperparameters and five-fold cross validation were tested in order to determine the set of hyperparameters that maximized the performance of the model. The number of trees in each forest was varied from 20 to 210 and the trees were split from 5 to 125 times. Both mean signed error and mean absolute error were considered when determining the quality of each split and between three and 14 features were examined when considering the best split. The optimized random forest model was then re-fit to the training data to validate the hyperparameter optimization. The RMSE of the random forest model decreased from 0.344 to 0.272 after optimization. The RMSE of the 1-hexene to 1-octene selectivities are 0.275 and 0.269, respectively.

The middle of Fig. 3 plots the selectivities determined from the optimized random model against those determined from the DFT selectivity model. In our data set, overall 1-hexene selective (*i.e.* >50% 1-hexene *vs.* 1-octene) is labeled as a negative value and overall 1-octene selective is labeled as a positive value (*i.e.* >50% 1-octene *vs.* 1-hexene). The random forest model correctly predicted the overall 1-hexene *versus* 1-octene selectivity for 83 ligands and incorrectly predicted the overall selectivity for 22 ligands. This incorrect assignment occurs in cases where the DFT computed 1-hexene selectivity of a ligand is less than 1%. The random forest model tends to perform best for ligands ranging from 20 : 80 to 50 : 50 1-hexene : 1-octene selectivity (see ESI-Fig. 1†). Importantly, the majority of ligands in our data set are overall 1-octene selective, which is useful for our goal of improving the percentage of 1-octene, but it is likely that the RMSE of the random forest model would be reduced if the data set were more evenly distributed between overall 1-hexene and overall 1-octene selective.

At the top and the bottom of Fig. 3, the 1-octene selectivities calculated using the DFT selectivity model and the optimized random forest model are plotted against the experimentally determined selectivities. The DFT selectivity model agreed with experiment very well (R^2 = 0.91, mean absolute deviation = 4.4%). The DFT model underestimates the experimental selectivity, however, this is overall advantageous with the goal to increase 1-octene production. In contrast to the DFT calculated values, the random forest model, not unexpectedly, is unable to quantitatively reproduce the experimental selectivities with a high degree of linear correlation. The lack of very high quantitative correlation between random forest and experiment values is likely due to the relatively small sample size of experimentally studied ligands. Despite this, the random forest can be used to determine critical chemical features that are responsible for enhancing 1-octene selectivity. The relative importance of the 14 features included in our dataset can be determined by replacing data with random values and observing the impact on the RMSE value. If replacing data of a feature with random values results in a small change to the RMSE then it has a low degree of importance. Conversely, if there is a large change in the RMSE then this feature has a large importance. Fig. 4 displays this feature importance analysis using the optimized random forest model.

Inspection of Fig. 4 shows that the Cr–N distance, Cr–α distance, and distance out of pocket were identified as being most important in enhancing 1-octene selectivity. The Cr–N–C_2 angle, which is related to the Cr–α distance, was also identified

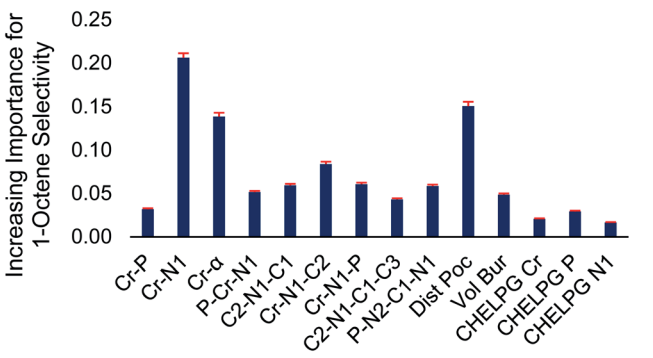

Fig. 4 Normalized feature importance determined from random forest model with 95% confidence intervals (red bars).

as an important 1-octene enhancing feature. Interestingly, despite the proposed importance of the ligand bite angle, especially for phosphine catalysts,[106] we found that the P–Cr–N_1 ligand bite angle is among several lesser important features, which is consistent with Sydora previously showing that for Cr-phosphinoamidine catalyst ligands with similar bite angles resulted in significantly different 1-hexene : 1-octene selectivities.[35] After we completed this machine learning analysis and identified the importance of the Cr-distance out of pocket for the 105 ligands examined here, Liu reported a DFT analysis of

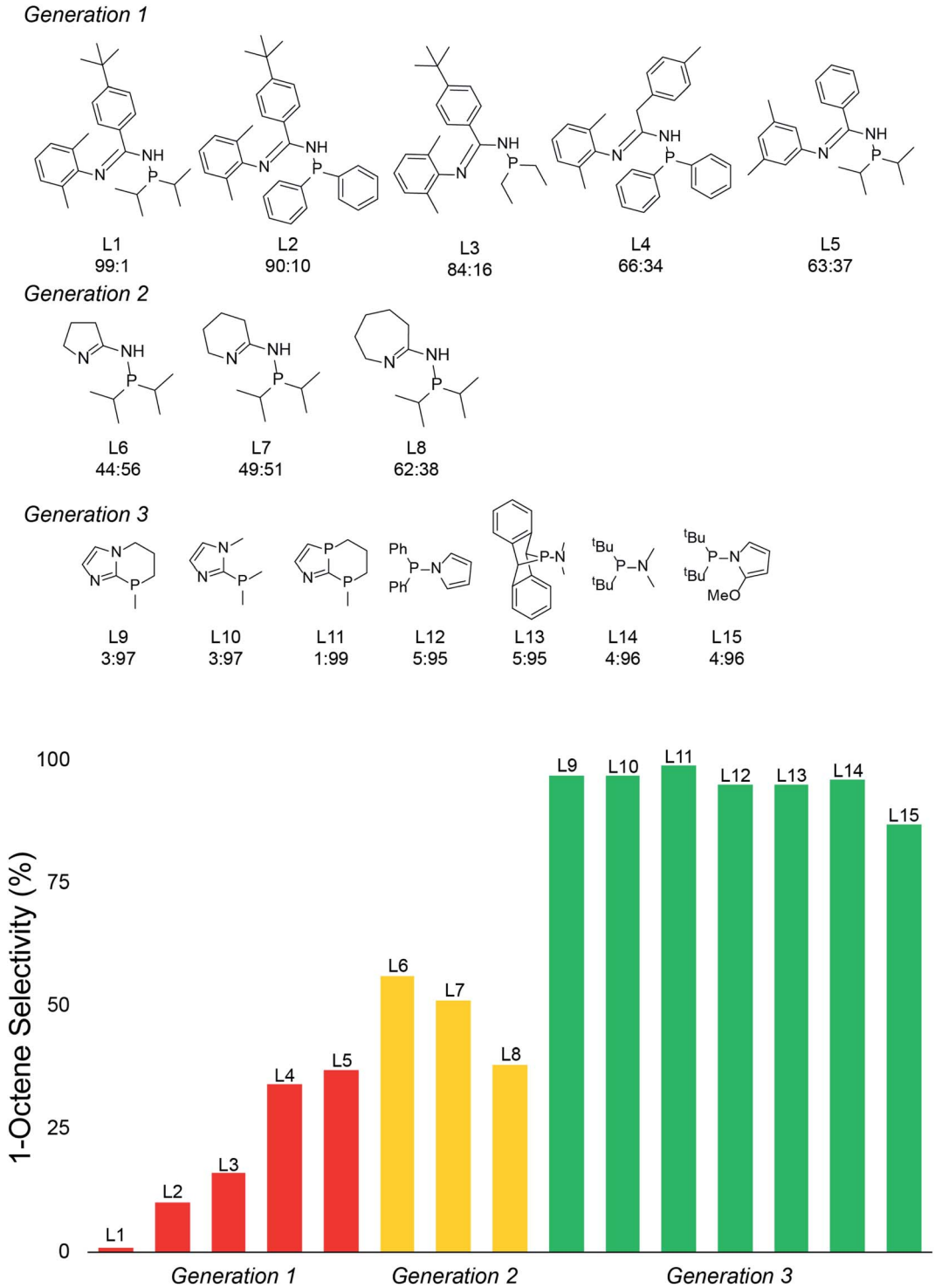

Fig. 5 Top: Structures for previous (P,N) ligand generations and the new proposed ligands (generation 3) based on machine-learning identified features. The 1-hexene : 1-octene selectivity (predicted) is given below each structure. Bottom: Plot of 1-octene selectivity for previous (P,N) ligand generations and new proposed ligands.

ethylene oligomerization by a Cr(2,2′-dipicolyamine) catalyst and also found that enhanced tetramerization was likely due to the Cr-distance out of pocket.

With the emergence of chemical features by the random forest machine learning model, we then turned to the final step in our workflow, which is using this information to virtually identify new catalyst ligands (Scheme 1c). Based on the important features, we rapidly designed ligands **L9–L15** shown in Fig. 5. The machine learning features directed us to change the 4-membered (P,N) ligand scaffold found in previously reported ligands of generations 1 (**L1–L5**) and 2 (**L6–L8**) to a 3-membered (P,N) ligand, which would potentially alter the Cr–N distance, Cr–α distance, and Cr distance out of ligand pocket. Briefly, generation 1 ligands were reported by Sydora[35] and based on experimental trial and error with only a single example of 1-octene production in the vicinity of 30%. Generation 2 ligands were computational designed by us using only transition-state energies, and then experimentally verified to show our DFT calculations were extremely accurate. However, this only led to the improvement of 1-octene selectivity to about 50%. Moreover, these transition states did not provide an obvious way to design a new, more selective generation of catalysts. Our machine-learning driven modification led to the proposal of ligands **L9–L11**, and with our transition-state model they are predicted to be 97–99% 1-octene selective. With the rapid success of this new generation 3 type of (P,N) ligands we further decreased the ligand to have direct phosphine-nitrogen connection, which naturally led to the proposal of 2-membered (P,N) ligands **L12–L14**. Based on our transition state model, ligands **L12–L14** have predicted selectivities of >95% for 1-octene. Importantly, as plotted at the bottom of Fig. 5, the use of our transition-state model combined with translation of machine learning features to new catalyst ligands, resulted in increasing the prediction of 1-octene from between <35% for generation 1 and ∼50% for generation 2 to >95% for generation 3.

With the rapid success of designing ligands **L9–L15** it is clear that there are a number of new candidates that are now available for experimental testing, and several more ligands can now be virtually and rapidly designed. As one experimental confirmation of our results, without prior knowledge, and subsequent to our design of **L9–L15**, a literature search of all reported Cr-phosphine catalysts for ethylene oligomerization revealed that Yang reported that **L12** is indeed highly 1-octene selective.[107] In this experimental test, which is signficantly different than the Chevron Phillips Chemical reaction conditions that our transition-state model was developed for, *in situ* catalyst formation with the combination of $Cr(acac)_3$, MAO, and **L12** oligomerized under 50 bar of ethylene gave a 1-hexene : 1-octene ratio of 28 : 70 with trace production of polyethylene.

Conclusions

For Cr(P,N) catalyzed ethylene oligomerization, we combined our previously developed experimentally verified DFT-transition-state model with a random forest machine learning model. This workflow involved the calculation of transition-state 1-hexene : 1-octene selectivity for 105 ligands and the harvesting of 14 descriptors, which were then used to build a random forest regression model with a low RMSE. This model revealed that Cr–N distance, Cr–α distance, and Cr distance out of pocket were key features for enhancing 1-octene selectivity. This then allowed the rapid design of several generation 3 Cr(P,N) catalyst ligands that are predicted to give >95% selectivity for 1-octene. Overall, this work demonstrated the utility of combining an accurate quantum-mechanical transition state model in tandem with machine learning to accelerate molecular catalyst design.

Conflicts of interest

A patent application has been filed for subject matter contained in this article.

Acknowledgements

We appreciate Dr Uriah Kilgore and Dr Brooke L. Small for helpful discussions during the preparation of this manuscript. We thank Brigham Young University and the Fulton Supercomputing Lab for computational resources. We thank Chevron Phillips Chemical Company LP for financial support and the opportunity to report these results.

References

1 D. H. Ess, L. Gagliardi and S. Hammes-Schiffer, *Chem. Rev.*, 2019, **119**, 6507–6508.
2 S. Ahn, M. Hong, M. Sundararajan, D. H. Ess and M.-H. Baik, *Chem. Rev.*, 2019, **119**, 6509–6560.
3 J. T. Golab, *CHEMTECH*, 1998, **28**, 17–23.
4 T. Sperger, I. A. Sanhueza and F. Schoenebeck, *Acc. Chem. Res.*, 2016, **49**, 1311–1319.
5 S. Hammes-Schiffer, *Acc. Chem. Res.*, 2017, **50**, 561–566.
6 C. Poree and F. Schoenebeck, *Acc. Chem. Res.*, 2017, **50**, 605–608.
7 C. Allemann, R. Gordillo, F. R. Clemente, P. H. Y. Cheong and K. N. Houk, *Acc. Chem. Res.*, 2004, **37**, 558–569.
8 K. N. Houk and P. H. Y. Cheong, *Nature*, 2008, **455**, 309–313.
9 D. J. Tantillo, *Angew. Chem., Int. Ed.*, 2009, **48**, 31–32.
10 R. B. Sunoj, *Wiley Interdiscip. Rev.: Comput. Mol. Sci.*, 2011, **1**, 920–931.
11 J. Jover and N. Fey, *Chem.–Asian J.*, 2014, **9**, 1714–1723.
12 Q. N. N. Nguyen and D. J. Tantillo, *Chem.–Asian J.*, 2014, **9**, 674–680.
13 A. S. K. Tsang, I. A. Sanhueza and F. Schoenebeck, *Chem.–Eur. J.*, 2014, **20**, 16432–16441.
14 D. J. Tantillo, *Acc. Chem. Res.*, 2016, **49**, 1079.
15 M. Kheirabadi, N. Çelebi-Ölçüm, M. F. L. Parker, Q. Zhao, G. Kiss, K. N. Houk and C. E. Schafmeister, *J. Am. Chem. Soc.*, 2012, **134**, 18345–18353.
16 A. C. Doney, B. J. Rooks, T. Lu and S. E. Wheeler, *ACS Catal.*, 2016, **6**, 7948–7955.
17 M. C. Kozlowski, S. L. Dixon, M. Panda and G. Lauri, *J. Am. Chem. Soc.*, 2003, **125**, 6614–6615.

18 J. C. Ianni, V. Annamalai, P. W. Phuan, M. Panda and M. C. Kozlowski, *Angew. Chem., Int. Ed.*, 2006, **45**, 5502–5505.
19 S. Mitsumori, H. Zhang, P. H. Y. Cheong, K. N. Houk, F. Tanaka and C. F. Barbas, *J. Am. Chem. Soc.*, 2006, **128**, 1040–1041.
20 G. Jindal and R. B. Sunoj, *Org. Biomol. Chem.*, 2014, **12**, 2745–2753.
21 Y. Wang, J. Wang, J. Su, F. Huang, L. Jiao, Y. Liang, D. Yang, S. Zhang, P. A. Wender and Z. X. Yu, *J. Am. Chem. Soc.*, 2007, **129**, 10060–10061.
22 P. J. Donoghue, P. Helquist, P. O. Norrby and O. Wiest, *J. Am. Chem. Soc.*, 2009, **131**, 410–411.
23 C. N. Rowley and T. K. Woo, *Can. J. Chem.*, 2009, **87**, 1030–1038.
24 M. H. Baik, S. Mazumder, P. Ricci, J. R. Sawyer, Y. G. Song, H. Wang and P. A. Evans, *J. Am. Chem. Soc.*, 2011, **133**, 7621–7623.
25 L. E. Fernandez, S. Horvath and S. Hammes-Schiffer, *J. Phys. Chem. Lett.*, 2013, **4**, 542–546.
26 M. C. Nielsen, K. J. Bonney and F. Schoenebeck, *Angew. Chem., Int. Ed.*, 2014, **53**, 5903–5906.
27 V. Bernales, A. B. League, Z. Li, N. M. Schweitzer, A. W. Peters, R. K. Carlson, J. T. Hupp, C. J. Cramer, O. K. Farha and L. Gagliardi, *J. Phys. Chem. C*, 2016, **120**, 23576–23583.
28 S. Tang, Z. Liu, X. Zhan, R. Cheng, X. He and B. Liu, *J. Mol. Model.*, 2014, **20**, 2129.
29 M. Karelson, V. S. Lobanov and A. R. Katritzky, *Chem. Rev.*, 1996, **96**, 1027–1043.
30 D. H. Kwon, J. T. Fuller, U. J. Kilgore, O. L. Sydora, S. M. Bischof and D. H. Ess, *ACS Catal.*, 2018, **8**, 1138–1142.
31 P. J. Hogan and R. L. Banks, in *History of Polyolefins: The World's Most Widley Used Polymers*, ed. R. B. Seymour and T. Cheng, Springer Netherlands, 1986, pp. 103–115.
32 G. Cecchin, G. Morini and F. Piemontesi, in *Kirk-Othmer Encyclopedia of Chemical Technology*, John Wiley and Sons, 2000.
33 A. Vaughan, D. S. Davis and J. R. Hagadorn, *J. Polym. Sci., Part A: Polym. Chem.*, 2012, **3**, 657–672.
34 K. A. Alferov, G. P. Belov and Y. Meng, *Appl. Catal., A*, 2017, **542**, 71–124.
35 O. L. Sydora, T. C. Jones, B. L. Small, A. J. Nett, A. A. Fischer and M. J. Carney, *ACS Catal.*, 2012, **2**, 2452–2455.
36 M. S. Sigman, K. C. Harper, E. N. Bess and A. Milo, *Acc. Chem. Res.*, 2016, **49**, 1292–1301.
37 P. Friederich, G. Dos Passos Gomes, R. De Bin, A. Aspuru-Guzik and D. Balcells, *Chem. Sci.*, 2020, **11**, 4584–4601.
38 N. Fey, A. C. Tsipis, S. E. Harris, J. N. Harvey, A. G. Orpen and R. A. Mansson, *Chem.–Eur. J.*, 2005, **12**, 291–302.
39 N. Fey, J. N. Harvey, G. C. Lloyd-Jones, P. Murray, A. G. Orpen, R. Osborne and M. Purdie, *Organometallics*, 2008, **27**, 1372–1383.
40 N. Fey, A. G. Orpen and J. N. Harvey, *Coord. Chem. Rev.*, 2009, **253**, 704–722.
41 J. Jover, N. Fey, J. N. Harvey, G. C. Lloyd-Jones, A. G. Orpen, G. J. J. Owen-Smith, P. Murray, D. R. J. Hose, R. Osborne and M. Purdie, *Organometallics*, 2010, **29**, 6245–6258.
42 J. Jover, N. Fey, J. N. Harvey, G. C. Lloyd-Jones, A. G. Orpen, G. J. J. Owen-Smith, P. Murray, D. R. J. Hose, R. Osborne and M. Purdie, *Organometallics*, 2012, **31**, 5302–5306.
43 D. J. Durand and N. Fey, *Chem. Rev.*, 2019, **119**, 6561–6594.
44 N. Fey, M. Garland, J. P. Hopewell, C. L. McMullin, S. Mastroianni, A. G. Orpen and P. G. Pringle, *Angew. Chem., Int. Ed.*, 2012, **51**, 118–122.
45 A. F. Zahrt, J. J. Henle, B. T. Rose, Y. Wang, W. T. Darrow and S. E. Denmark, *Science*, 2019, **363**, eaau5631.
46 K. E. Abdelfatah, W. Yang, R. Vijay Solomon, B. Rajbanshi, A. Chowdhury, M. Zare, S. K. Kundu, A. C. Yonge, A. Heyden and G. A. Terejanu, *J. Phys. Chem. C*, 2019, **123**, 29804–29810.
47 K. Takahashi and I. Miyazato, *J. Comput. Chem.*, 2018, **39**, 2405–2408.
48 A. R. Singh, B. A. Rohr, J. A. Gauthier and J. K. Nørskov, *Catal. Lett.*, 2019, **149**, 2347–2354.
49 H.-J. Arpe, *Industrial Organic Chemistry*, Wiley-VCH Verlag GmbH & Co, 5th edn, 2010.
50 PCT/US2006/031303, 2008.
51 P.-A. R. Breuil, L. Magna and H. Olivier-Bourbigou, *Catal. Lett.*, 2015, **145**, 173–192.
52 G. J. P. Britovsek and D. S. McGuinness, *Chem.–Eur. J.*, 2016, **22**, 16891–16896.
53 G. J. P. Britovsek, D. S. McGuinness and A. K. Tomov, *Catal. Sci. Technol.*, 2016, **6**, 8234–8241.
54 S. A. Bartlett, J. Moulin, M. Tromp, G. Reid, A. J. Dent, G. Cibin, D. S. McGuinness and J. Evans, *ACS Catal.*, 2014, **4**, 4201–4204.
55 T. Agapie, *Coord. Chem. Rev.*, 2011, **255**, 861–880.
56 M. A. Hossain, H. S. Kim, K. N. Houk and M. Cheong, *Bull. Korean Chem. Soc.*, 2014, **35**, 2835–2838.
57 Z. X. Yu and K. N. Houk, *Angew. Chem., Int. Ed.*, 2003, **42**, 808–811.
58 M. Gong, Z. Liu, Y. Li, Y. Ma, Q. Sun, J. Zhang and B. Liu, *Organometallics*, 2016, **35**, 972–981.
59 Y. Yang, Z. Liu, R. Cheng, X. He and B. Liu, *Organometallics*, 2014, **33**, 2599–2607.
60 Y. Qi, Q. Dong, L. Zhong, Z. Liu, P. Qiu, R. Cheng, X. He, J. Vanderbilt and B. Liu, *Organometallics*, 2010, **29**, 1588–1602.
61 P. H. M. Budzelaar, *Can. J. Chem.*, 2009, **87**, 832–837.
62 S. Bhaduri, S. Mukhopadhyay and S. A. Kulkarni, *J. Organomet. Chem.*, 2009, **694**, 1297–1307.
63 W. J. Van Rensburg, C. Grové, J. P. Steynberg, K. B. Stark, J. J. Huyser and P. J. Steynberg, *Organometallics*, 2004, **23**, 1207–1222.
64 M. A. Kayala, C. A. Azencott, J. H. Chen and P. Baldi, *J. Chem. Inf. Model.*, 2011, **51**, 2209–2222.
65 J. N. Wei, D. Duvenaud and A. Aspuru-Guzik, *ACS Cent. Sci.*, 2016, **2**, 725–732.
66 H. Gao, T. J. Struble, C. W. Coley, Y. Wang, W. H. Green and K. F. Jensen, *ACS Cent. Sci.*, 2018, **4**, 1465–1476.

67 C. W. Coley, W. H. Green and K. F. Jensen, *Acc. Chem. Res.*, 2018, **51**, 1281–1289.
68 B. Liu, B. Ramsundar, P. Kawthekar, J. Shi, J. Gomes, Q. Luu Nguyen, S. Ho, J. Sloane, P. Wender and V. Pande, *ACS Cent. Sci.*, 2017, **3**, 1103–1113.
69 C. W. Coley, R. Barzilay, T. S. Jaakkola, W. H. Green and K. F. Jensen, *ACS Cent. Sci.*, 2017, **3**, 434–443.
70 D. T. Ahneman, J. G. Estrada, S. Lin, S. D. Dreher and A. G. Doyle, *Science*, 2018, **360**, 186–190.
71 W. Sun, M. Li, Y. Li, Z. Wu, Y. Sun, S. Lu, Z. Xiao, B. Zhao and K. Sun, *Adv. Theory Simul.*, 2019, **2**, 1800116.
72 C. W. Coley, W. Jin, L. Rogers, T. F. Jamison, T. S. Jaakkola, W. H. Green, R. Barzilay and K. F. Jensen, *Chem. Sci.*, 2019, **10**, 370–377.
73 A. Tomberg, M. J. Johansson and P. O. Norrby, *J. Org. Chem.*, 2019, **84**, 4695–4703.
74 A. F. Zahrt, J. J. Henle, B. T. Rose, Y. Wang, W. T. Darrow and S. E. Denmark, *Science*, 2019, **363**, 6424.
75 S. Back, K. Tran and Z. W. Ulissi, *ACS Catal.*, 2019, **9**, 7651–7659.
76 G. Takasao, T. Wada, A. Thakur, P. Chammingkwan, M. Terano and T. Taniike, *ACS Catal.*, 2019, **9**, 2599–2609.
77 Z. W. Ulissi, M. T. Tang, J. Xiao, X. Liu, D. A. Torelli, M. Karamad, K. Cummins, C. Hahn, N. S. Lewis, T. F. Jaramillo, K. Chan and J. K. Nørskov, *ACS Catal.*, 2017, **7**, 6600–6608.
78 A. Nandy, J. Zhu, J. P. Janet, C. Duan, R. B. Getman and H. J. Kulik, *ACS Catal.*, 2019, **9**, 8243–8255.
79 X. Zhu, J. Yan, M. Gu, T. Liu, Y. Dai, Y. Gu and Y. Li, *J. Phys. Chem. Lett.*, 2019, **10**, 7760–7766.
80 A. J. Chowdhury, W. Yang, E. Walker, O. Mamun, A. Heyden and G. A. Terejanu, *J. Phys. Chem. C*, 2018, **122**, 28142–28150.
81 B. R. Goldsmith, J. Esterhuizen, J. X. Liu, C. J. Bartel and C. Sutton, *AIChE J.*, 2018, **64**, 2311–2323.
82 X. Guo, S. Lin, J. Gu, S. Zhang, Z. Chen and S. Huang, *ACS Catal.*, 2019, **9**, 11042–11054.
83 X. Han, L. Yue, C. Zhao, S. Jiang, J. Liu, Y. Li and J. Ren, *ChemistrySelect*, 2019, **4**, 11790–11795.
84 R. Jinnouchi and R. Asahi, *J. Phys. Chem. Lett.*, 2017, **8**, 4279–4283.
85 J. Ohyama, S. Nishimura and K. Takahashi, *ChemCatChem*, 2019, **11**, 4307–4313.
86 R. Palkovits and S. Palkovits, *ACS Catal.*, 2019, **9**, 8383–8387.
87 K. Takahashi, I. Miyazato, S. Nishimura and J. Ohyama, *ChemCatChem*, 2018, **10**, 3223–3228.
88 G. A. Landrum, J. E. Penzotti and S. Putta, *Meas. Sci. Technol.*, 2005, **16**, 270–277.
89 B. A. Rizkin and R. L. Hartman, *Chem. Eng. Sci.*, 2019, **210**, 115224.
90 J. P. Janet and H. J. Kulik, *Chem. Sci.*, 2017, **8**, 5137–5152.
91 J. P. Janet and H. J. Kulik, *J. Phys. Chem. A*, 2017, **121**, 8939–8954.
92 B. Meyer, B. Sawatlon, S. Heinen, O. A. Von Lilienfeld and C. Corminboeuf, *Chem. Sci.*, 2018, **9**, 7069–7077.
93 S. Banerjee, A. Sreenithya and R. B. Sunoj, *Phys. Chem. Chem. Phys.*, 2018, **20**, 18311–18318.
94 A. Mansouri Tehrani, A. O. Oliynyk, M. Parry, Z. Rizvi, S. Couper, F. Lin, L. Miyagi, T. D. Sparks and J. Brgoch, *J. Am. Chem. Soc.*, 2018, **140**, 9844–9853.
95 G. X. Gu, C. T. Chen and M. J. Buehler, *Extreme Mech. Lett.*, 2018, **18**, 19–28.
96 Z. Li, X. Ma and H. Xin, *Catal. Today*, 2017, **280**, 232–238.
97 Y. Zhao and D. G. Truhlar, *Theor. Chem. Acc.*, 2008, **120**, 215–241.
98 A. V. Marenich, C. J. Cramer and D. G. Truhlar, *J. Phys. Chem. B*, 2009, **113**, 6378–6396.
99 M. J. Frisch, G. W. Trucks, H. B. Schlegel, G. E. Scuseria, M. A. Robb, J. R. Cheeseman, G. Scalmani, V. Barone, B. Mennucci, G. A. Petersson, H. Nakatsuji, M. Caricato, X. Li, H. P. Hratchian, A. F. Izmaylov, J. Bloino, G. Zheng and J. L. Sonnenberg, 2009.
100 E. Jones, T. Oliphant and P. Peterson, *SciPy: Open source scientific tools for Python*, 2001.
101 T. Oliphant, *A Guide to NumPy*, Trelgol Publishing, USA, 2006.
102 W. McKinney, in *Proceedings of the 9th Python in Science Conference*, ed. S. van der Walt and J. Millman, 2010, pp. 51–56.
103 F. Pedregosa, G. Varoquaux, A. Gramfort, V. Michel, B. Thirion, O. Grisel, M. Blondel, P. Prettenhofer, R. Weiss, V. Dubourg, J. Vanderplas, A. Passos, D. Cournapeau, M. Brucher, M. Perrot and E. Duchesnay, *J. Mach. Learn. Res.*, 2011, **12**, 2825–2830.
104 L. Falivene, Z. Cao, A. Petta, L. Serra, A. Poater, R. Oliva, V. Scarano and L. Cavallo, *Nat. Chem.*, 2019, **11**, 872–879.
105 D. S. Palmer, N. M. O'Boyle, R. C. Glen and J. B. O. Mitchell, *J. Chem. Inf. Model.*, 2007, **47**, 150–158.
106 S.-K. Kim, T.-J. Kim, J.-H. Chung, T.-K. Hahn, S.-S. Chae, H.-S. Lee, M. Cheng and S. O. Kang, *Organometallics*, 2010, **29**, 5805–5811.
107 Y. Yang, Z. Liu, B. Liu and R. Duchateau, *ACS Catal.*, 2013, **3**, 2353–2361.